

# Superpixel-Based Image Segmentation Using Squared 2-Wasserstein Distances

Jisui Huang<sup>1,2</sup>, Andreas Alpers<sup>1\*</sup>, Ke Chen<sup>4\*</sup>, Na Lei<sup>5</sup>

<sup>1</sup>Department of Mathematical Sciences, Centre for Mathematical Imaging Techniques (CMIT), University of Liverpool, Peach Street, Liverpool, L697ZL, Merseyside, United Kingdom.

<sup>2</sup>School of Mathematical Sciences, Capital Normal University, West Third Ring Road North, Haidian District, Beijing, 100084, China.

<sup>4</sup>Department of Mathematics and Statistics, University of Strathclyde, Richmond St, Glasgow, G11XH, Scotland, United Kingdom.

<sup>5</sup>DUT-RU International School of Information Sciences & Engineering, Dalian University of Technology, Linggong Road, Dalian, 116024, Liaoning, China.

## Abstract

We present an efficient method for image segmentation in the presence of strong inhomogeneities. The approach can be interpreted as a two-level clustering procedure: pixels are first grouped into superpixels via a linear least-squares assignment problem, which can be viewed as a special case of a discrete optimal transport (OT) problem, and these superpixels are subsequently greedily merged into object-level segments using the squared 2-Wasserstein distance between their empirical distributions. In contrast to conventional superpixel merging strategies based on mean-color distances, our framework employs a distributional OT distance, yielding a mathematically unified formulation across both clustering levels. Numerical experiments demonstrate that this perspective leads to improved segmentation accuracy on challenging images while retaining high computational efficiency.

**Keywords:** discrete optimal transport, clustering, Voronoi diagrams, anisotropic power diagrams, selective segmentation, unsupervised segmentation

# 1 Introduction

Image segmentation is a fundamental task in image processing and computer vision, which aims at partitioning an image into parts that share common semantic features. Variational models [1–4] are efficient framework for image segmentation as long as the image is approximately piecewise smooth. They represent the object boundary as an implicit contour of the level set function, then assign each level set an energy, and finally minimize a functional to obtain the segmentation. Variational models typically comprise a region term and an edge term.

The region term typically measures the fidelity of the segmentation to the observed image [5]. In the Chan–Vese model [6], each region is approximated by its mean intensity, yielding an efficient piecewise-constant formulation. However, this global variance assumption limits its ability to handle intensity inhomogeneities. Consequently, numerous extensions have been proposed to incorporate spatially varying image models [7–10]. Examples include local averaging schemes [7], bias-field estimation [11], Gaussian statistical models [10], and combined local–global priors [12].

The edge term typically enforces contour smoothness by penalizing geometric fluctuations. In the geodesic active contour model [13], this is achieved by minimizing a gradient-weighted length functional, which attracts the contour toward image boundaries. Since pure gradients are sensitive to noise, many extensions broaden the notion of edge information. Examples include multi-local statistical gradients [14], adaptive perturbation mechanisms [15], and curvature-based regularization. Euler’s elastica has been shown to complete missing boundaries [16], while Ricci-curvature-based formulations [17, 18] replace the gradient norm with intrinsic geometric descriptors for improved robustness.

However, current level set models still face two challenges. The first problem is intensity inhomogeneity. An early attempt extended the Chan–Vese model [6] to the multi-phase version [19], which, however, might divide both the foreground and background into several different parts. Recently, the local region descriptor [7, 20, 21] has been exploited to displace the traditional global mean. For example, the local binary fitting term [8] incorporates the weighted distance between the original image and the local averaged image. However, local information cannot distinguish fine features from noise. The coupled denoising term used in [22] could also not eradicate this inherited drawback. Another approach is to decompose the image into fluctuation and homogeneity fields and segment the homogeneity part only. Li et al. [11] optimized an additional bias field to correct the biased image mean. Zhang et al. [23] simultaneously used a bias field, mean and variance to describe a region. However, the bias field is typically evaluated using local information, such as the convolution, which may not be robust to noise.

A second major limitation is the high computational cost of level-set-based models. Region terms typically require updating region statistics at every iteration, ranging from simple mean estimates in Chan–Vese [6] to convolution-based local descriptors [7–10]. Edge-based formulations often lead to second-order PDEs [24], which are commonly solved using iterative methods such as gradient-descent or semi-implicit schemes [25]. Curvature regularisation introduces even higher-order Euler–Lagrange equations, as in Elastica-based models [16]. Moreover, practical implementations

require periodic reinitialization of the level-set function to maintain a signed-distance representation [26, 27], adding further computational overhead.

To overcome these problems, we introduce an efficient superpixel-based segmentation method that remains robust under strong global inhomogeneity, in both unsupervised and marker-guided settings. Pixels are first grouped into homogeneous superpixels (see [28]), providing boundary-preserving regions on which all computations are performed. Similarity between superpixels is measured using the squared 2-Wasserstein distance from OT [29], which seems inherently robust to global intensity variation and weak boundaries. The segmentation is then obtained by greedily minimising a regularised pairwise OT energy over the region-adjacency graph, explicitly tracking the evolving mixtures of superpixels. Operating entirely at the superpixel level yields substantial computational savings compared with pixel-based variational models.

Most superpixel-based level-set methods incorporate superpixel-derived features into the level-set function to guide segmentation, but still rely on a pixel-level representation [30–37]. Other approaches use superpixels primarily to accelerate subsequent processing [38–40], yet their heterogeneity measures—typically differences of means or variances—are too coarse for complex intensity inhomogeneity. In contrast, the squared 2-Wasserstein distance provides robustness to global intensity disturbances. Although the method in [41] also employs a Wasserstein metric, it requires reference distributions derived from ground-truth data, limiting its applicability. Our approach is fully unsupervised and does not rely on ground-truth distributions.

Our contribution is summarised as follows:

- A two-level OT formulation of segmentation, unifying superpixel construction and region merging within a single OT perspective.
- A distributional region similarity measure based on the squared 2-Wasserstein distance, replacing mean-based and variance-based descriptors.
- A superpixel-level optimization strategy that avoids pixel-grid PDEs by evolving mixtures of superpixels on the region-adjacency graph.
- A fully unsupervised OT-driven method that does not require reference distributions and is robust to strong global inhomogeneity.

Related OT-based region-merging ideas, without superpixels or Wasserstein distances, appeared earlier in a conference paper by the present authors [42].

The paper is organized as follows. Section 2 introduces the notation and mathematical background. Section 3 reviews related segmentation models. Section 4 presents our superpixel model, and Section 5 describes the corresponding optimization algorithm. Sections 6–7 report numerical comparisons on synthetic and real images. Conclusions appear in Section 8.

## 2 Notation and Mathematical Background

We denote by  $\mathbb{R}^d$  the  $d$ -dimensional Euclidean space with the standard Euclidean norm  $\|\cdot\|$ , and by  $\mathbb{R}_{\geq 0}$  the set of nonnegative real numbers. We model an image as a function  $I : \Omega \rightarrow \mathbb{R}^c$ , with  $\Omega \subseteq \mathbb{R}^d$  denoting the spatial domain. Gray-level images

correspond to the case  $c = 1$ , whereas color images typically have  $c = 3$ . For  $x \in \Omega$ , we write  $I(x) = (I_1(x), \dots, I_c(x))^T$  for its channel components. We will refer to elements  $x \in \Omega$  as pixel locations, even when the ambient dimension  $d$  is not restricted to 2; when no confusion can arise, we will simply write pixels. This is a continuous model. A discretized image is a representation of an image  $I$  as a discrete  $\mathbb{R}^c$ -valued measure supported on a finite set of pixel locations. Formally, it is given by

$$I = \sum_{y \in \Omega'} I(y) \delta(\cdot - y),$$

where  $\Omega' \subseteq \Omega$  is a finite set of pixels,  $I(y) \in \mathbb{R}^c$  denotes the color at pixel  $y$ , and  $\delta(\cdot - y)$  denotes the Dirac measure concentrated at  $y$ . In this formulation,  $I$  is a discrete measure concentrated at the points of  $\Omega'$ . We denote by  $\mathbb{1}_n \in \mathbb{R}^n$  the vector with all entries equal to one, and by  $\chi_V$  the indicator function of a set  $V$ , defined as  $\chi_V(x) = 1$  if  $x \in V$ , and  $\chi_V(x) = 0$  otherwise.

## 2.1 Histograms

Let  $I : \Omega \rightarrow \mathbb{R}^c$  be an image and  $\widehat{\Omega} \subseteq \Omega$  a region. Let  $\{c_1, \dots, c_k\} \subseteq \mathbb{R}^c$  be a set of predefined bin centers, and define the associated Voronoi cells (bins) by

$$V_i = \{z \in \mathbb{R}^c \mid \|z - c_i\| \leq \|z - c_j\| \text{ for all } j \neq i\}, \quad i = 1, \dots, k.$$

The (normalized) histogram  $v_{\widehat{\Omega}} = (\nu_1, \dots, \nu_k)^T$  of a region  $\widehat{\Omega} \subseteq \Omega$ , with respect to the image  $I$  and the bin centers  $\{c_1, \dots, c_k\}$ , is then defined by

$$\nu_i = \frac{\int_{\widehat{\Omega}} \chi_{V_i}(I(x)) dx}{\int_{\widehat{\Omega}} dx},$$

where  $\chi_{V_i} : \mathbb{R}^c \rightarrow \{0, 1\}$  denotes the indicator function of the Voronoi cell  $V_i$ . The histogram  $v_{\widehat{\Omega}}$  can be viewed as the discrete measure  $\sum_{i=1}^k \nu_i \delta(\cdot - c_i)$  supported on the bin centers.

## 2.2 Optimal Transport

Let  $v \in \mathbb{R}_{\geq 0}^a$ ,  $w \in \mathbb{R}_{\geq 0}^b$  satisfy the balance equation  $v^T \mathbb{1}_a = w^T \mathbb{1}_b$ . The *transportation polytope associated with  $v$  and  $w$*  is defined by

$$\mathcal{P}(v, w) := \left\{ P = (p_{ij})_{i,j} \in \mathbb{R}_{\geq 0}^{a \times b} \mid P \mathbb{1}_b = v, P^\top \mathbb{1}_a = w \right\}.$$

Transportation polytopes are well-studied objects in polyhedral geometry; we refer to [43] for a survey of their combinatorial and geometric properties.

Transportation polytopes appear in a variety of computational and optimization settings. From the OT perspective, transportation polytopes can be used to model mass-preserving couplings between measures. For further background on OT, we refer to the monographs [44–46].

In OT, the *(balanced) Kantorovich problem* consists in solving

$$\min_{P \in \mathcal{P}(v, w)} \sum_{i=1}^a \sum_{j=1}^b d_{ij} p_{ij},$$

where  $(d_{ij})_{i,j}$  is a prescribed cost matrix. This is a linear program, whose solution represents an optimal transport plan between supplies  $v$  and demands  $w$ , where  $p_{ij}^*$  specifies the amount transported from index  $i$  to index  $j$ .

Two special cases are worth mentioning. First, if  $v = \mathbb{1}_a$ , the feasible set  $\mathcal{P}(\mathbb{1}_a, w)$  corresponds to a *(fractional) assignment problem* in which each supply node is assigned exactly once, while demand nodes admit multiple assignments according to their capacities  $w_j$ . Second, if  $v^T \mathbb{1}_a = w^T \mathbb{1}_b = 1$ , the vectors  $v$  and  $w$  can be interpreted as discrete probability measures (histograms) supported on bin centers  $\{c_i\}_{i=1}^a \subseteq \mathbb{R}^c$  and  $\{c'_j\}_{j=1}^b \subseteq \mathbb{R}^c$ , respectively. For the quadratic cost

$$d_{ij} := \|c_i - c'_j\|^2,$$

we define

$$d(v, w) := \left( \min_{P \in \mathcal{P}(v, w)} \sum_{i=1}^a \sum_{j=1}^b \|c_i - c'_j\|^2 p_{ij} \right)^{1/2}. \quad (1)$$

The quantity  $d(v, w)$  is the *2-Wasserstein distance* between  $v$  and  $w$  and defines a metric on the space of discrete probability measures. In the following, we primarily work with the squared distance  $d^2(v, w)$ , corresponding to the quadratic OT cost, which is more convenient in our setting. With a slight abuse of notation, we also write  $d(\Omega_i, \Omega_j)$  for the 2-Wasserstein distance between the histograms associated with the regions  $\Omega_i$  and  $\Omega_j$  of  $I$ .

### 3 Related Work and Segmentation Models

Building on this notion of region comparison, we now turn to segmentation models that aim at robustness to noise and intensity inhomogeneities.

#### 3.1 Variational Methods

A variety of variational models have been proposed in the literature to specifically address intensity inhomogeneity and high noise levels; however, to our knowledge, none of them are superpixel-based. Among them, the Ali-Rada (AR) [22] and Zhang-Zhang (ZZ) [23] models can be viewed as state-of-the-art approaches. Both can be seen as advancements of the classical Local Binary Fitting (LBF) model [8], which we will first review. To facilitate the explanation, we will present the models for the two-phase case, where the primary goal is to segment the image into foreground and background. We denote the Heaviside function by  $H : \mathbb{R} \rightarrow \mathbb{R}$ , defined by  $H(x) = 0$  for  $x < 0$  and  $H(x) = 1$  for  $x > 0$ , and we denote by  $\phi : \Omega \rightarrow \mathbb{R}$  the level set

function used to partition the image into foreground  $\{x \in \Omega : \phi(x) > 0\}$ , background  $\{x \in \Omega : \phi(x) < 0\}$ , and contour  $\{x \in \Omega : \phi(x) = 0\}$ .

### 3.1.1 Local Binary Fitting (LBF) Model

The LBF model [8], replacing the constant image intensity means of the classical Chan-Vese model [6] by adaptive functions  $f_1, f_2 : \Omega \rightarrow \mathbb{R}^c$  optimizes

$$\begin{aligned} & \arg \min_{\phi, f_1, f_2} \lambda_1 \int_{\Omega} K(x-y) \|I(y) - f_1(x)\|^2 H(\phi(y)) \, dx \, dy \\ & + \lambda_2 \int_{\Omega} K(x-y) \|I(y) - f_2(x)\|^2 (1 - H(\phi(y))) \, dx \, dy \\ & + \mu \int_{\Omega} \delta(\phi(x)) \|\nabla \phi(x)\| \, dx \\ & + \nu \int_{\Omega} \frac{1}{2} (\|\nabla \phi(x)\| - 1)^2 \, dx, \end{aligned}$$

where  $\lambda_1, \lambda_2, \mu, \nu > 0$  are fixed parameters and  $K$  is the Gaussian kernel  $K(x-y) = \exp(-\|x-y\|^2/2\sigma^2)$  with standard deviation  $\sigma$ . The first two terms of the model can be viewed as region terms, aiming at fitting image intensities. The  $\mu$ -term aims at minimizing contour length, while the  $\nu$ -term resembles a signed distance function.

Optimal functions  $f_1, f_2$ , for given  $\phi$ , can be derived from variational calculus:

$$f_1(x) = \frac{\int_{\Omega} K(x-y) H(\phi(y)) I(y) \, dy}{\int_{\Omega} K(x-y) H(\phi(y)) \, dy}, \quad f_2(x) = \frac{\int_{\Omega} K(x-y) (1 - H(\phi(y))) I(y) \, dy}{\int_{\Omega} K(x-y) (1 - H(\phi(y))) \, dy}.$$

Note that, in the two-dimensional case, the region terms involve four-dimensional integrals. It is also known that the LBF model can be sensitive to initialization [21].

### 3.1.2 Ali-Rada (AR) Model

Given the two spatially varying average functions  $f_1, f_2$  in the LBF model, a statistically locally computed approximation  $\bar{I}$  of the image  $I$  can be defined via

$$\bar{I}(x) = f_1(x) H(\phi(x)) + f_2(x) (1 - H(\phi(x))).$$

The AR model [22], utilizing a combination of this locally computed denoising constrained surface and a denoising fidelity term, optimizes

$$\begin{aligned} & \arg \min_{\phi, f_1, f_2} \lambda \int_{\Omega} \|I(x) - \bar{I}(x)\|^2 \, dx \\ & + (1 - \lambda) \int_{\Omega} \sum_{k=1}^c \left( \log(\bar{I}_k(x)) + I_k(x)/\bar{I}_k(x) \right) \, dx \\ & + \mu \int_{\Omega} \delta(\phi(x)) \|\nabla \phi(x)\| \, dx, \end{aligned}$$

where  $\mu > 0$  and  $\lambda \in [0, 1]$  are given constants.

### 3.1.3 Zhang-Zhang (ZZ) Model

The ZZ model [23] also employs local information to mitigate the effect of inhomogeneities. Introducing an unknown bias field  $B : \Omega \rightarrow \mathbb{R}$ , it is assumed that the intensities in a neighborhood of a pixel follow a Gaussian distribution, yielding the model

$$\begin{aligned} \arg \min_{\phi, B, c_1, c_2, \sigma_1, \sigma_2} & \int_{\Omega} K_{\rho}(x-y) \left( \log(\sigma_1) + \frac{\|I(y) - B(x)c_1\|^2}{2\sigma_1^2} \right) H(y) dx dy \\ & + \int_{\Omega} K_{\rho}(x-y) \left( \log(\sigma_2) + \frac{\|I(y) - B(x)c_2\|^2}{2\sigma_2^2} \right) (1 - H(y)) dx dy \\ & + \mu \int_{\Omega} \delta(\phi(x)) \|\nabla \phi(x)\| dx, \end{aligned}$$

where  $\mu > 0$  is a given constant and  $K_{\rho}$  denotes the characteristic function of the radius- $\rho$  ball. The rationale for incorporating  $c_1, c_2 \in \mathbb{R}^c$  and  $\sigma_1, \sigma_2 \in \mathbb{R}$  lies in modeling the intensities around the foreground pixel  $x$  as a Gaussian distribution with mean  $B(x)c_1$  and standard deviation  $\sigma_1$ , while for background pixels  $x$ , the intensities are modeled by a Gaussian distribution with mean  $B(x)c_2$  and standard deviation  $\sigma_2$ .

## 3.2 Deep Learning Models: The Segment Anything Model (SAM)

Another class of models is given by deep learning models. The past few years have witnessed a surge in deep learning models for image segmentation. Among these models, SAM, introduced in 2023 [47], stands out as a state-of-the-art method that has been pre-trained on an extensive dataset of over 1 billion masks across 11 million images. At its core, SAM utilizes a vision transformer architecture [48]. In this work, we employ SAM's zero-shot capability to perform object segmentation without requiring prior training on the objects in the image. We apply SAM in both prompted and non-prompted modes, where the prompts function as marker points to assist the model in identifying and segmenting the objects of interest. Recent performance evaluations of the SAM model can be found in [49–51].

## 3.3 Superpixel-based Segmentation Models

Superpixel algorithms group pixels with similar color and other low-level properties. They are increasingly incorporated into image segmentation algorithms, see, e.g., [30–40]. Among these approaches, the SMST model from [38] is the most methodologically similar to our proposed model. Consequently, we provide a brief overview of SMST and include it in our comparison. We begin with a summary of the superpixel generation methods SLIC and Power-SLIC, underlying SMST and our approach, respectively.

### 3.3.1 Superpixel Generation: SLIC

Among the methods available for superpixel generation (see [52, 53] for a comprehensive evaluation), SLIC [54], an adaptation of the  $k$ -means clustering method [55, 56] for superpixel generation, stands out as one of the most popular and widely used techniques. Given a discretized image of  $N$  pixels, SLIC clusters pixels in the joint spatial–feature space  $\mathbb{R}^d \times \mathbb{R}^c$ , where each pixel  $p$  is represented by  $(x_p, I(x_p))$ , with  $I(x_p)$  taking values in CIELAB space [57] for color images and in  $\mathbb{R}$  for grayscale images.

The algorithm comprises two main phases. In the first phase, SLIC depends on two parameters,  $m$  and  $\alpha$ , where  $m$  specifies the target number of superpixels and  $\alpha$  is a compactness parameter ( $\alpha = 10$  is common in 2D). The cluster centers are initialized on a regular grid with spacing  $h = \sqrt{N/m}$ . During the assignment step, each pixel is compared only to cluster centers within a spatial neighborhood of size proportional to  $h$ . The similarity between a pixel  $p$  and a cluster center  $s$  is measured by the weighted squared Euclidean distance

$$\text{dist}^2(p, s) = \|x_p - x_s\|^2 + \frac{h^2}{\alpha^2} \|I(x_p) - I(x_s)\|^2.$$

As in  $k$ -means, the centers are updated as the centroids of the updated clusters, and the process is iterated until some stopping criterion is fulfilled. In a second phase, connectivity is enforced by relabeling small disconnected components to adjacent superpixels.

### 3.3.2 Superpixel Generation: Power-SLIC

In our proposed method, we will employ a recent superpixel generation method called Power-SLIC [28]. This method improves over SLIC in terms of speed, noise robustness, and compactness. Conceptually, Power-SLIC computes, heuristically, a solution of the fractional assignment problem discussed in Section 2.2.

More specifically, Power-SLIC first computes pixel subsets  $C_j$ ,  $j = 1, \dots, m$ , via the first phase of SLIC. Then a principal component analysis is performed, i.e., for each  $j$ , the sample covariance matrix  $\Sigma_j$ , the centroid  $c(C_j)$ , and the cardinality  $|C_j|$  of the data set  $C_j$  are calculated. Setting  $A_j := \Sigma_j^{-1}$ , this defines an ellipsoidal norm  $\|\cdot\|_{A_j}$  via  $\|x\|_{A_j} := \sqrt{x^T A_j x}$ . If one then solves the fractional assignment problem from Section 2.2 with  $a = N$ ,  $b = m$ ,  $w_j = |C_j|$ , and quadratic costs  $d_{ij} = \|x_i - c(C_j)\|_{A_j}^2$ , for  $i = 1, \dots, N$  and  $j = 1, \dots, m$ , then its dual linear problem yields parameters  $\mu_1^*, \dots, \mu_m^*$ , which define cells

$$V_i := \{x \in \Omega : \|x - c(C_i)\|_{A_i}^2 - \mu_i^* \leq \|x - c(C_j)\|_{A_j}^2 - \mu_j^*, \quad \text{for all } j = 1, \dots, m\};$$

see [28] for details. The  $m$ -tuple  $(V_1, \dots, V_m)$  of cells is referred to in the literature as *anisotropic power diagram* or *generalized balanced power diagram* [58, 59]. These possess an inherent geometric structure, generalizing the concepts of *Voronoi* and *Laguerre diagrams* (see, e.g., [60]). The discrete superpixels are then the sets  $V_i \cap \Omega'$ ,  $i =$

$1, \dots, m$ . To reduce computational complexity, Power-SLIC uses a heuristic parameter update and sets

$$\mu_i^* := \left( \frac{|C_i|}{\kappa_d} \sqrt{\det(A_i)} \right)^{2/d},$$

with  $\kappa_d$  denoting the volume of the  $d$ -dimensional unit ball; see [61] for a discussion of the underlying rationale in the context of discriminant analysis.

### 3.3.3 Superpixel-based Minimum Spanning Tree (SMST) Model

Superpixel-based segmentation methods frequently employ a combination of merging and splitting phases. The SMST model described in [38] constitutes a state-of-the-art example of this paradigm.

The SMST model performs the segmentation in four stages. First, superpixels are generated via SLIC. The superpixels are represented as nodes in a graph, with edges weighted by the dissimilarity between nodes, and a minimum spanning tree is then computed based on this graph. Second, superpixels are gradually merged using the MST structure (the implementation uses the approach from [62]). During the merging several key parameters, such as the inter-cluster variance, are calculated and monitored. In a third stage, the parameters are analyzed to yield an estimate of the number of objects in the image. In the fourth stage, the superpixels are split to generate the initial MST, and re-merging is carried out until the determined number of objects is reached.

## 4 Proposed SP (Superpixel) Model

Our model, which we refer to as the *SP (superpixel) model*, is a greedy, adjacency-constrained, OT-based energy-minimization model formulated on the region-adjacency graph of an initial superpixel partition. Let  $\mathcal{Q}_m = \{\Omega_1, \dots, \Omega_m\}$  denote an oversegmentation of the discretized image  $I$  into  $m$  nonempty superpixels, and let  $v_{\Omega_i}$  denote the histogram associated with region  $\Omega_i$ ; see Section 2.1. We consider the region-adjacency graph  $G = (V, E)$ ,  $V = \{1, \dots, m\}$ , where  $(i, j) \in E$  if and only if  $\Omega_i$  and  $\Omega_j$  share a common boundary. For each adjacent pair  $(i, j) \in E$ , we define the dissimilarity  $E_{ij} = d^2(v_{\Omega_i}, v_{\Omega_j})$ , the squared 2-Wasserstein distance between their color histograms; see (1).

To each region  $\Omega_i$  we associate a heterogeneity value  $h_i$ , initialized as  $h_i = 0$ . Whenever two regions  $\Omega_i$  and  $\Omega_j$  are merged, we update  $h_i \leftarrow E_{ij}$ , so that  $h_i$  records the most recent merge cost involving  $\Omega_i$ . The *regularized merge cost* associated with merging adjacent regions  $\Omega_i$  and  $\Omega_j$  is then defined as

$$\kappa_{ij} = E_{ij} - h_i - h_j. \quad (2)$$

The rationale behind this construction is to encourage merges that are both locally coherent in color distribution and consistent with the hierarchical structure of previously merged regions. The heterogeneity terms  $h_i$  act as a memory mechanism that penalizes merges that are locally incompatible with the merge history.

A segmentation with  $n < m$  regions is described by a sequence of admissible merges  $\mathcal{M} = ((i_1, j_1), \dots, (i_{m-n}, j_{m-n}))$ , where each  $(i_k, j_k)$  is an adjacent pair in the current region-adjacency graph. For such a merge sequence  $\mathcal{M}$ , we define the *regularized pairwise optimal-transport energy*

$$\mathcal{E}_{\text{reg}}(\mathcal{M}) = \sum_{k=1}^{m-n} \left( d^2(v_{\Omega_{i_k}}, v_{\Omega_{j_k}}) - h_{i_k} - h_{j_k} \right),$$

with the heterogeneity values  $h_i$  evolving according to the update rule above. The SP model is the global minimization problem

$$\arg \min_{\mathcal{M} \in \mathfrak{A}_{m \rightarrow n}} \mathcal{E}_{\text{reg}}(\mathcal{M}),$$

where  $\mathfrak{A}_{m \rightarrow n}$  denotes the set of all admissible merge sequences reducing the initial partition  $\mathcal{Q}_m$  to a partition of size  $n$ .

## 5 SP Optimization Algorithms

We next introduce three algorithmic variants of the SP model, corresponding to different assumptions on the available input information.

### 5.1 Unsupervised SP Algorithm

The unsupervised SP algorithm takes as input an image  $I$ , a prescribed number of initial superpixels  $m \in \mathbb{N}$ , a target number of regions  $n \leq m$ , and a number  $k \in \mathbb{N}$  of color representatives used in the histogram computations. Given these inputs, the algorithm constructs an initial partition of  $I$  into  $m$  superpixels via Power-SLIC and then iteratively merges regions until exactly  $n$  remain.

To approximately minimize the SP model, we employ a greedy region-merging strategy. At each iteration, among all adjacent region pairs  $(i, j)$ , the algorithm selects the pair that minimizes the regularized merge cost  $\kappa_{ij}$  (see (2)). The region  $\Omega_j$  is merged into  $\Omega_i$ , the heterogeneity value is updated according to  $h_i \leftarrow E_{ij}$ , and the region-adjacency graph is updated accordingly. This greedy procedure yields a hierarchy of progressively coarser partitions that provides an efficient approximation to a minimizer of the regularized OT energy  $\mathcal{E}_{\text{reg}}$ . The full unsupervised SP optimization algorithm is summarized in Algorithm 1.

### 5.2 SP Algorithm with Automatic Region Number Selection

Algorithm 1 can be extended to automatically determine the number of regions from the evolution of the merging process. The algorithm is run until a single region remains, yielding a sequence of merges. At each iteration, two regions  $\Omega_i$  and  $\Omega_j$  minimizing the regularized merge cost  $\kappa_{ij}$  (see (2)) are merged, and we define

$$\text{LT}(r) := d^2(\Omega_i, \Omega_j),$$

---

**Algorithm 1** Unsupervised SP optimization algorithm

---

**Require:** Discretized image  $I$ , number of superpixels  $m \in \mathbb{N}$ , number  $n \leq m$  of objects, number of color representatives  $k \in \mathbb{N}$ .

**Ensure:** Partition  $\{\Omega_i : \Omega_i \neq \emptyset\}$  of  $I$  into  $n$  superpixel regions.

- 1: Compute  $k$  representative colors of  $I$  for histogram-based distance computations.
- 2: Partition  $I$  into  $m$  nonempty superpixels  $\Omega_1, \Omega_2, \dots, \Omega_m$  using Power-SLIC.
- 3: Initialize region heterogeneity levels  $h_i \leftarrow 0$  for all  $i = 1, \dots, m$ .
- 4: Initialize  $E_{ij} \leftarrow d^2(\Omega_i, \Omega_j)$  for all adjacent region pairs  $i < j$ .
- 5: Initialize a priority queue  $Q$  with entries

$$(E_{ij} - h_i - h_j, i, j)$$

for all adjacent region pairs  $i < j$ .

- 6: Set  $r \leftarrow m$ .
- 7: **while**  $r > n$  **do**
- 8:     Extract  $(\kappa, i, j) \in Q$  with minimal key  $\kappa$ .
- 9:     **if**  $(\Omega_i \neq \emptyset \text{ and } \Omega_j \neq \emptyset)$  **then**
- 10:         Merge  $\Omega_j$  into  $\Omega_i$ .
- 11:          $h_i \leftarrow E_{ij}$ .
- 12:          $r \leftarrow r - 1$ .
- 13:          $\text{LT}(r) \leftarrow h_i$ . ▷ Used only when  $n$  is determined via ROC-LT.
- 14:         **for** each region  $\Omega_k$  adjacent to  $\Omega_i$  **do**
- 15:             Recompute  $E_{ik} \leftarrow d^2(\Omega_i, \Omega_k)$ .
- 16:             Insert  $(E_{ik} - h_i - h_k, i, k)$  into  $Q$ .
- 17:         **end for**
- 18:     **end if**
- 19: **end while**

---

where  $r$  denotes the number of regions after merging. The resulting sequence  $\{\text{LT}(r)\}$  records the costs of successive merges as  $r$  decreases. Following the rate-of-change (ROC) criteria introduced and motivated in [38, 63], we consider the relative discrete variation  $\text{ROC}(r) = (\text{LT}(r-1) - \text{LT}(r)) / \text{LT}(r)$ , whose local maximizers  $r^*$  indicate suitable values of  $n$  (selected by visual inspection in all experiments in this paper). The corresponding partition is obtained by reversing the final  $n-1$  merges.

### 5.3 Marker-Based (Supervised) SP Algorithm

When user-specified markers  $(p_i, I_i)$  are available, Algorithm 1 replaces the prescribed number of regions by marker locations  $p_i$  with associated classes  $I_i$ , assuming exactly  $n$  distinct classes.

After superpixel initialization (line 2), marker regions  $M = \{M_I\}_I$  are defined as unions of initial superpixels containing markers of class  $I$ .

In lines 4 and 15, the dissimilarity  $d^2(\Omega_i, \Omega_j)$  is replaced by a marker-aware dissimilarity  $d_M^2(\Omega_i, \Omega_j)$ , which defines region dissimilarity relative to a class-specific

reference region in the presence of a unique marker class. It is given by

$$d_M^2(\Omega_i, \Omega_j) := d^2(\Omega_i, C(\Omega_i, \Omega_j)) + d^2(\Omega_j, C(\Omega_i, \Omega_j)),$$

where

$$C(\Omega_i, \Omega_j) := \begin{cases} M_I, & \text{if } \Omega_i \cup \Omega_j \text{ contains markers of exactly one class } I, \\ \Omega_i, & \text{otherwise.} \end{cases}$$

Moreover, the loop condition is amended to  $r > n$  and  $Q \neq \emptyset$ . Finally, the merge condition  $\Omega_i \neq \emptyset$  and  $\Omega_j \neq \emptyset$  is strengthened by requiring that all markers contained in  $\Omega_i \cup \Omega_j$  belong to the same class. Note that the output is a partition of  $I$  into superpixel regions consistent with the prescribed marker classes; however, the number of regions is not fixed a priori and may exceed the number of classes.

#### 5.4 Computational Cost

We analyze Algorithm 1 in the unit-cost RAM model (see, e.g., [64, 65]), assuming standard implementations of priority queues (binary heaps) and adjacency lists, with region merges performed using standard representative-based bookkeeping. The superpixel partition induces a region adjacency graph with  $E$  edges and  $m$  vertices. We further assume that each pixel color can be assigned to one of the  $k$  representative colors in constant time, for instance via a precomputed lookup table built during the representative-color computation. Let  $T_{\text{rep}}(N, k)$  denote the worst-case running time required to compute the  $k$  representative colors in our image  $I$  containing  $N$  pixels, and let  $T_{\text{OT}}(k)$  denote the worst-case running time required to solve a balanced transportation problem of size at most  $k$ .

**Proposition 1** *Algorithm 1 runs in worst-case time*

$$O(T_{\text{rep}}(N, k) + N + m^2 \log m + E T_{\text{OT}}(k) + mk).$$

*Proof* The algorithm consists of an initialization phase followed by a merging loop.

Computing  $k$  representative colors takes  $T_{\text{rep}}(N, k)$  time. Superpixelization of  $I$  via Power-SLIC, including histogram initialization, requires  $O(N)$  time, while initializing region heterogeneity levels takes  $O(m)$ . For each adjacent region pair, one distance  $d(\Omega_i, \Omega_j)$  is evaluated and inserted into the priority queue, yielding a total cost of  $O(E T_{\text{OT}}(k))$  for distance computations and  $O(E)$  queue insertions.

The main loop performs  $m - n$  merge operations. The worst case occurs for  $n = 1$ , which we therefore analyze. A single merge operation consists of merging the two regions as sets, merging their adjacency information, and merging the associated histograms with  $k$  bins.

When two regions are merged, they are removed, and a new, larger region is formed. Distance computations and priority queue insertions are performed for all adjacent pairs involving the newly formed region and its  $O(m)$  neighbors, yielding a total cost of  $O(m^2 T_{\text{OT}}(k))$  for distance recomputations and  $O(m^2)$  priority queue insertions overall, each costing  $O(\log(m))$ .

Each merge incurs an  $O(k)$  cost for histogram updates. As at most  $m - 1$  merges are performed, the total cost of histogram updates is  $O(mk)$ .

Unsuccessful extractions from the priority queue discard stale entries and do not affect the asymptotic running time.

Combining these bounds yields the stated worst-case running time.  $\square$

The superpixel adjacency graph typically induces a planar subdivision and therefore satisfies  $E = O(m)$  by classical bounds for simple planar graphs (see, e.g., [66]). In contrast, for a general graph one only has the trivial bound  $E = O(m^2)$ .

Balanced transportation problems with  $k$  supply and  $k$  demand nodes can be solved in strongly polynomial time in the unit-cost RAM model; see, for example, the cost-scaling algorithm [67]. In our implementation, the distance computations  $d(\Omega_i, \Omega_j)$  are carried out using the network simplex-based optimal transport solver of Bonneel et al. [68, 69]. While this solver does not admit a known polynomial worst-case complexity bound, it is empirically observed to exhibit near-quadratic running time in many practical instances [68]. In all experiments reported below, we fix  $k = 15$ .

Concerning the term  $T_{\text{rep}}(N, k)$ , our implementation computes representative colors from an auxiliary Power-SLIC partition into a fixed number of regions (300 in all experiments). Color vectors are averaged within each auxiliary region, and the  $k$  representative colors are selected as the  $k$  most frequent averages. Since the number of auxiliary regions is fixed, this procedure can be implemented in  $O(N)$  time, and hence  $T_{\text{rep}}(N, k) = O(N)$  in our setting.

Combining the planarity assumption  $E = O(m)$  with the implementation-specific specializations above, and noting that  $k$  is fixed in all experiments, the effective worst-case running time of Algorithm 1 simplifies to  $O(N + m^2 \log m)$ .

## 6 Numerical Experiments

In this section, we evaluate the quality and efficiency of our model under intensity inhomogeneities. For comparison, we include the following models:

- **SP**: our SP model (optimized via Algorithm 1 and variants; see Section 5),
- **AR**: the Ali-Rada model [22],
- **ZZ**: the Zhang-Zhang model [23],
- **SMST**: the superpixel-based minimum spanning tree model [38], and
- **SAM**: the Segment Anything model [47].

We next describe the implementation details and computational settings for the models under comparison.

SP is implemented in C++ incorporating the network simplex solver [69] for OT computations. The MATLAB code is (obtained by compiling the C++ code into MEX modules) is available at [GitHub](#). As remarked before, we use  $k = 15$  color representatives in all experiments.

For the AR and ZZ models, we employ the level-set framework of [25], which uses additive operator splitting (AOS) with convex relaxation and avoids explicit reinitialization. AOS decomposes each 2-D Laplacian update into two 1-D tridiagonal solves. The original implementation relies on MATLAB's generic solver `mldivide`,

which does not exploit this structure, so we replace it with the linear-time Thomas algorithm [70]. In the ZZ model, we reformulate the quadruple integral as a set of 2D convolutions, reducing the cost from quadratic to quasi-linear using FFT acceleration.

The SMST model is implemented in C++ using a minimum-spanning-tree representation together with a custom implementation of the REDCAP procedure [62] as no public implementation is available. Subtree variances are expressed via  $\text{var}(X) = \mathbb{E}[X^2] - \mathbb{E}[X]^2$ , so that all required statistics reduce to sums of  $X$ ,  $X^2$ , and region areas over subtree nodes. A depth-first traversal linearizes the tree, mapping each subtree to a contiguous memory interval and enabling all aggregates to be computed by prefix sums; the interval structure is updated after each bipartition.

The SAM model was executed on Google Colab using a Tesla T4 GPU. All other models were run on a Lenovo laptop equipped with a 13th-generation Intel(R) Core(TM) i9-13900HX CPU and 40 GB RAM.

## 6.1 Datasets

We evaluate three datasets exhibiting challenges typical in microscopy and biomedical imaging, including illumination variability, heterogeneous object morphology, large object counts, and regional intensity inhomogeneity.

**Dataset 1** comprises a synthetic video and two hematoxylin and eosin (H&E)-stained images collected from public online sources [71, 72]. H&E staining is standard in histopathology, with nuclei appearing blue–purple and cytoplasm pink. The images are provided in RGB format with varying image sizes and are used solely for qualitative illustration and timing comparisons, as no ground-truth annotations are available. The synthetic video consists of 74 MATLAB-generated frames. The first frame shows a 3D mitochondrial mesh generated via the `isosurface` function and rendered with Phong illumination, with the light source positioned above and to the right of the camera. Subsequent frames are obtained by rotating this initial view. This dataset was constructed to study segmentation under pronounced frame-to-frame illumination changes.

**Dataset 2**, released as supplementary material in [73], contains 36 digitized H&E-stained microscopy images ( $600 \times 600$  pixels) with 7931 nuclei annotated by three expert pathologists; only consensus annotations are retained. It is designed for cell nuclei detection.

**Dataset 3** consists of 50 annotated H&E-stained histological images from triple-negative breast cancer patients [74]. The images were acquired at  $40\times$  magnification using a Philips Ultra Fast Scanner (1.6RA) at the Curie Institute and contain a total of 4022 annotated cells.

Representative samples from the three datasets are shown in Fig. 1. In (a), the first frame of the synthetic video in Dataset 1 illustrates the strong illumination gradients produced by distance-dependent shading together with orientation-dependent interactions between vertex normals and the light direction. The H&E images in (b) and (c), also from Dataset 1, depict a mast cell infiltrate from a patient with non-alcoholic steatohepatitis and cirrhosis and, respectively, a sample from a patient with sclerosing polycystic adenosis of the parotid gland; the former consists primarily of purple nuclei, white cytoplasm, and pink extracellular tissue. Subfigures (d) and (e)

show two examples from Dataset 2 accompanied by their ground-truth nuclei annotations, while (f) and (g) present a representative image from Dataset 3 together with its corresponding cell mask.

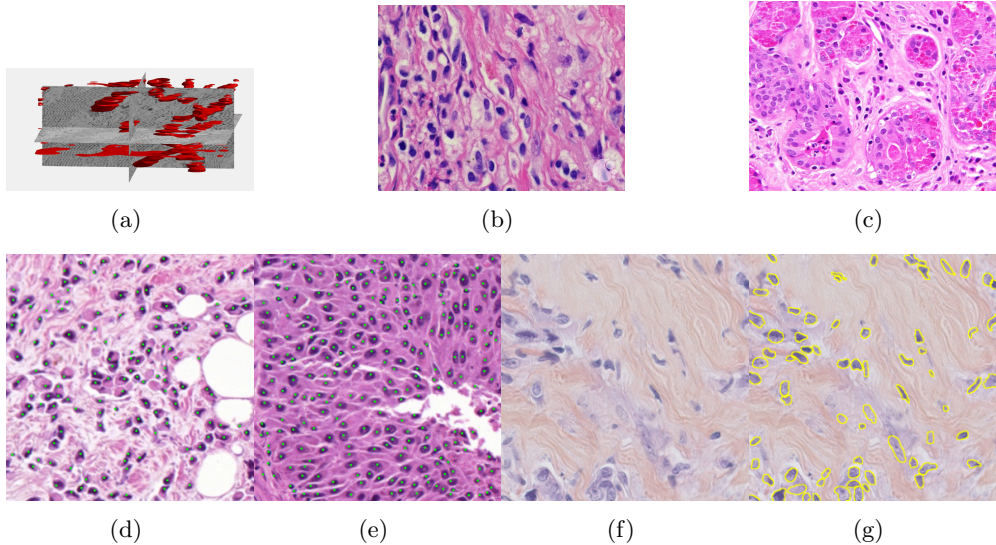


**Fig. 1:** Samples from Datasets 1–3. (a) First frame of the 74-frame video in Dataset 1 ( $1770 \times 880$ ) with a superimposed red mesh. (b,c) H&E-stained tissue images from Dataset 1 ( $1000 \times 750$ ;  $950 \times 730$ ). (d,e) Cell images from Dataset 2 ( $600 \times 600$ ) with nuclei annotations. (f,g) Image from Dataset 3 ( $512 \times 512$ ) with annotation.

## 7 Results

In this section, we present both qualitative and quantitative evaluations of the proposed method in comparison with established approaches. The analysis addresses segmentation accuracy under varying conditions, computational performance, and the influence of user interaction.

### 7.1 Qualitative Results

We first investigate qualitative aspects of the segmentations.

#### 7.1.1 Optimal Number of Segmentation Regions

Based on the image in Fig. 1b, we demonstrate how the ROC mechanism can identify the optimal number of segmentation regions. The LT and ROC–LT curves for this image are shown in Figs. 2a–2b, respectively. The curves show only minor fluctuations for region numbers below 162 indicating that suitable segmentations are

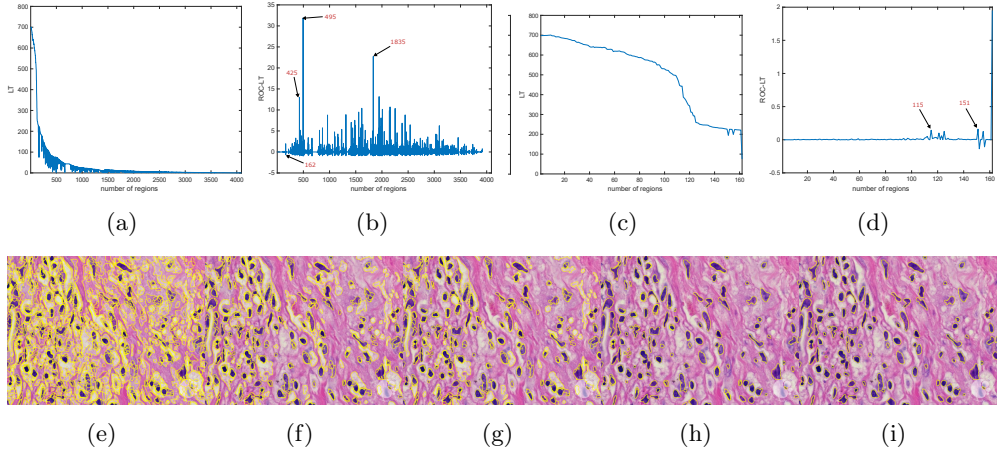


**Fig. 2:** Selection of the optimal number of regions. The LT curve (a) shows a general decrease with minor fluctuations, while the ROC-LT curve (b) remains essentially zero over  $[1, 162]$ , suggesting an optimal region number below 162. Zoomed views (c, d) reveal peaks at 115 and 151. Segmentations with 1835, 495, 425, 151, and 115 regions are shown in (e–i).

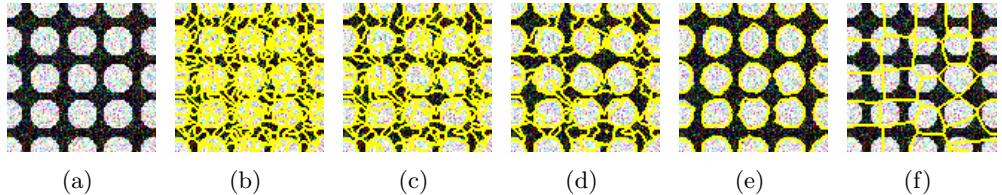


**Fig. 3:** Segmentation vs. Oversegmentation. (a) Noisy grayscale image containing 25 white objects. (b) Power-SLIC result with 300 superpixels, serving as input to our algorithm. (c–e) Intermediate and final steps of the algorithm, merging into 200, 100, and finally 25 regions, respectively. (f) Power-SLIC output with 25 superpixels.

likely to lie within the interval  $[1, 162]$ . Within this range (Figs. 2c–2d), local optima seem to lie at 115 and 151, suggesting these as plausible object counts. Segmentation results corresponding to the local maxima in the higher region interval  $[162, 4000]$  result in over-segmented images (Figs. 2e to 2g). The segmentation into 151 regions (Fig. 2h) reveals closely spaced, potentially redundant boundaries, which are resolved by the merging into 115 regions (Fig. 2i). This 115-region segmentation preserves clear foreground–background separation and can therefore be viewed as optimal solution.

### 7.1.2 Segmentation vs. Oversegmentation

Next, we compare the results of the baseline oversegmentation algorithm Power-SLIC with those obtained after applying our merging procedure. Fig. 3a presents a noisy

grayscale image containing 25 disks, some of which are partially occluded. We initialized our method by generating 300 superpixels using Power-SLIC (Fig. 3b); these superpixels conform to disk boundaries while retaining regular shapes in homogeneous regions. The algorithm then iteratively merged adjacent superpixels, yielding the intermediate results shown in Figs. 3c-3d and the final segmentation depicted in Fig. 3e. By contrast, considering only the raw superpixel output for 25 superpixels as segmentation is unsatisfactory (Fig. 3f).

### 7.1.3 OT vs. Variance

To assess the contribution of the OT-based metric in isolation, we substituted the superpixel initialization with a uniform rectangular partition and compared the outcome to that of the SMST algorithm. Since SMST also employs an initial superpixel decomposition followed by minimum-spanning-tree merging and variance-based splitting, any discrepancies can be attributed solely to the choice of metric.

Figure 4 shows, in its first row, two representative images from Dataset 1, overlaid with uniform rectangular partitions of varying resolution. Since the task was to segment red cells, only the red channels of the images were provided to both models. The second row of the figure presents the segmentation results from SP. Despite the rectangular initialization, our approach captured foreground regions using the smallest boxes possible while adhering to the rectangle boundaries. The third row of Fig. 4 shows the SMST results, which detected fewer cells and, across all resolutions, tended to over-segment the background into multiple regions.

### 7.1.4 Selective Models

We now evaluate SP’s selective segmentation (Section 5.3) by specifying markers and their class membership. Several level set models, such as the Roberts–Chen model [25] and the AR model, provide graphical interfaces that allow users to place seeds or draw regions marking the objects of interest. Some deep learning models, such as SAM, also support semantic selective segmentation.

Figure 5 shows an image from Dataset 3 with two different sets of markers. In the first case, Fig. 5(a,b), we manually placed five foreground seeds and one background seed; in the second case, Fig. 5(c,d), we slightly perturb the position of makers to test the stability of different models. Foreground and background seeds are labeled with the prefixes ‘f’ and ‘b,’ respectively, with the following number indicating their order (e.g., f2 denotes the second foreground seed). Note that there is only one background seed b1 in both cases. We then provided these to AR, SAM, and SP as markers.

Our model SP follows the selective variant from Section 5.3, with the target region number set equal to the number of markers. For SAM, we used the selective segmentation module in MATLAB 2024b. The AR model, while not requiring explicit background seeds, still needed background information; this was provided by assuming the domain outside the specified foreground was background. Since AR expects polygonal regions rather than points, we dilated the foreground seeds with a disk kernel and used the resulting regions as markers.

Figure 6 shows the results for the first case (Fig. 5a) with incrementally added foreground markers. SAM performed well with 1-2 markers, but with 4-5 it incorrectly

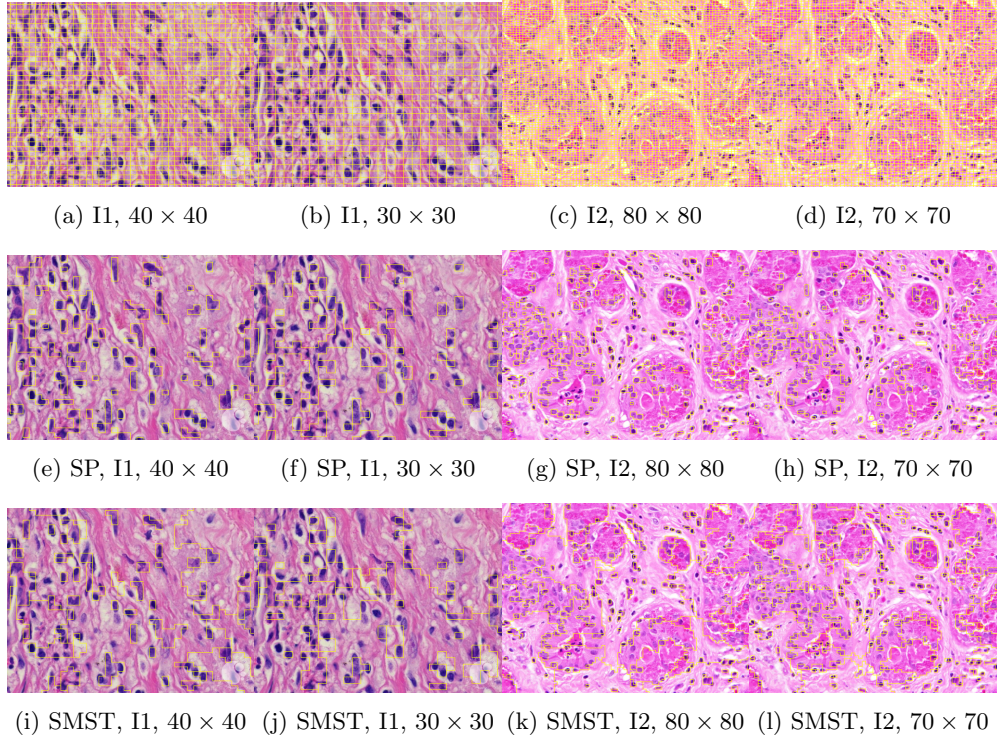


**Fig. 4:** Comparison of OT-based segmentation and variance-based SMST. The first row (a–d) shows two images I1 and I2 from Dataset 1 partitioned into rectangular superpixels of sizes  $40 \times 40$  (a),  $30 \times 30$  (b),  $80 \times 80$  (c), and  $70 \times 70$  (d), respectively. The second row (e–h) shows SP results (times in seconds: 1.97, 0.28, 22.48, 16.12). The third row (i–l) shows SMST results (times in seconds: 0.35, 0.35, 0.37, 0.43).

classified much of the domain as foreground suggesting that the scattered markers led SAM to infer that the entire image was of interest. AR produced a clear background but failed to segment the cells containing f1, f3, and f5, while adding an extra cell around f4. By contrast, SP consistently captured all marked cells while maintaining a clean background.

Figure 7 shows the results for the second case, the case with slightly perturbed marker positions (Fig. 5c). Similar to the previous scenario, SAM performed successfully only on the cell with the first foreground marker, while for the other marker, SAM mixed the target cell with other structures. AR showed similar problems as before, recognising only the first two cells (f1 and f2) and disregarding the others. This occurred because, during iterations, AR incorrectly shrank the level set corresponding to the other markers. The results for SP are identically to those in Fig. 6 and are therefore not duplicated in this figure.

In summary, AR and SAM seem sensitive to both the position and number of markers, whereas SP yields consistent results despite marker perturbations, benefiting

from noise-robust superpixels and an OT metric that is comparatively insensitive to such variability.

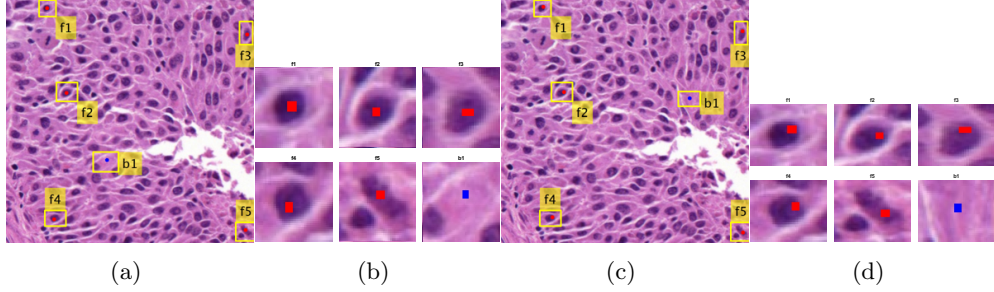


**Fig. 5:** Selective segmentation seeds: (a,c) images with foreground (red) and background (blue) seeds, labeled ‘f’ and ‘b’ respectively (numbers indicate order); (b,d) corresponding zoomed-in views.

### 7.1.5 Unsupervised Models

We validate unsupervised SP on the three datasets by comparison with SAM, SMST, AR, and ZZ. All methods are fully unsupervised; however, AR and ZZ require an initial level set for contour evolution.

We first present segmentation results for Dataset 1. Figures 8c-8g show the outputs for the image in Fig. 1a, for SAM, AR, ZZ, SMST, and SP. The AR and ZZ models used manually specified initial level sets (Fig. 8a), while SP and SMST used the same set of 4000 superpixels generated by Power-SLIC (Fig. 8b) using the first two LAB channels. SAM relied solely on RGB images. The segmentation goal was to separate the red mesh from the grayscale background. SAM omitted some meshes and introduced background noise; AR and ZZ misclassified many dark meshes as background due to their reliance on local region terms; the SMST method erroneously classified portions of the foreground as background and produced a fragmented representation of the background region. In contrast, SP achieved accurate segmentation of all meshes while successfully suppressing the background. Computation times are as follows: SMST was fastest (0.42s + 0.38s for Power-SLIC and merging), followed by SP (0.42s + 4.45s for Power-SLIC and merging). SAM required 14.62s (including model loading), while ZZ was the slowest at 11102.89s, requiring a substantial number of pixel level convolutions and iterations in the employed additive operator splitting (AOS) scheme; see [25].

Figure 9 shows the segmentation results for the first hematoxylin and eosin (H&E)-stained image from Dataset 1 (see Fig. 1b). Initial level sets and superpixels are shown in Figs. 9a-9c: AR and ZZ used two distinct level sets for nuclei (S1) and cytoplasm (S2) (Figs. 9a-9b), while SP and SMST (Fig. 9c) used the same set of 4000 Power-SLIC superpixels in the same color space (red channel for S1, remaining channels for S2). SAM does not allow separate-channel segmentation; its combined S1/S2

result is shown in Fig. 9d. Figures 9e-9h display S1 results for AR, ZZ, SMST, and SP, and Figs. 9i-9l show the corresponding S2 results.

AR seemed highly sensitive to initialization, segmenting mainly regions near seed points and requiring seeds in nearly all connected foreground components for satisfactory performance. ZZ segmented a wider range of objects from fewer seeds but incorrectly included nuclei in cytoplasm segmentation, failing to capture white regions and introducing spurious tissue. SAM automatically detected many nuclei and some cytoplasm but merged all structures into a single segmentation, limiting its practical utility here. SMST was the fastest but failed to recover large homogeneous regions, such as the background, and frequently fragmented them due to its variance-based metric. In contrast, SP yielded the most accurate results on both S1 and S2, with clear background separation and precise boundary delineation.

Figure 10 shows the results for the second hematoxylin–eosin stained image from Dataset 1 (see Fig. 1c). The AR model detected only structures near the initialization, missing many objects. The ZZ model recovered most cells but also introduced numerous unnecessary pink regions, and its two outputs were nearly identical despite different initial level sets (Figs. 10a-10b), similar to the over-segmentation behavior of SAM (Fig. 10d). SAM, which does not require initialization, failed to separate different structures, while SMST produced too few foreground objects and added spurious regions, without a clear background. In contrast, SP, initialized with 6000 Power-SLIC superpixels (Fig. 10c), achieved accurate separation of nuclei and cytoplasm.

## 7.2 Quantitative Results

We now assess SP using the 36 images from Dataset 2 and 50 images from Dataset 3. In our evaluation, we employ the Dice similarity coefficient (DSC) (as usual defined as the harmonic mean of precision and recall),  $DSC = 2/(1/precision + 1/recall)$ , precision =  $tp/(tp + fp)$ , recall =  $tp/(tp + fn)$ , where  $tp$  denotes the number of ground-truth points within the segmentation foreground,  $fp$  the number of predicted regions without ground truth, and  $fn$  the number of ground-truth points outside the segmentation foreground [73]. In Dataset 3, since pixel-level annotations were given [74], the above metrics were calculated on a per-pixel basis.

To facilitate automatic comparison, we specify the parameters used for this task. For AR and ZZ in Dataset 2, initial level sets were created by applying morphological dilation to the first 40 ground-truth points using a disk-shaped kernel with a radius of 5. If fewer than 40 points were available, all available points were dilated instead. For AR and ZZ in Dataset 3, pixel-level ground truth was provided, and the ground truth was eroded using a disk-shaped kernel with a radius of 5 as manually drawing these initializations would be time-consuming. SAM, SP, and SMST treat each connected component as a single object; they do not explicitly distinguish foreground from background. Consequently, the largest connected component was designated as background, with all remaining regions assigned to the foreground. Furthermore, because SMST often fragments the background into multiple regions, we treated SMST output regions containing holes as background. To implement this, regions with an Euler number less than 1 were removed using MATLAB’s `regionprops` function.

		AR	SMST	ZZ	SAM	SP
Dataset 2	DSC	66.32	80.47	81.69	82.88	<b>88.78</b>
	Preproc. Time (s)	$\infty$	<b>0.08</b>	$\infty$	6.09	<b>0.08</b>
	Segm. Time (s)	395.81	<b>0.38</b>	2212.70	7.75	14.55
Dataset 3	DSC	61.35	60.63	65.33	73.00	<b>76.62</b>
	Preproc. Time (s)	$\infty$	<b>0.08</b>	$\infty$	6.65	<b>0.08</b>
	Segm. Time (s)	302.76	<b>0.39</b>	1758.84	7.54	16.47

**Table 1:** Quantitative comparison of segmentation accuracy (Dice coefficient, DSC) and running time on Dataset 2 and 3.

Table 1, on Dataset 2, shows that SP obtained the highest DSC (88.78), which is higher by 5.90, 7.09, 8.31, and 22.46 compared to SAM, ZZ, SMST, and AR, respectively. The segmentation time of SP was 14.55s, approximately twice that of SAM (the second fastest method without considering pre-processing times), and more than one order of magnitude lower than the level-set methods AR and ZZ. While AR and ZZ need user-specific markers as input (the pre-processing time indicated as  $\infty$ ), SAM needs to load the pre-trained model (6.09s) while SP and SMST need to generate the superpixels in the pre-processing step (0.08s). Figure 11 shows the resulting segmentations for two example images from Figs. 1d and 1e from Dataset 2. The segmentations reflect the trends observed in Table 1, with SP achieving the highest DSC and segmentation times exhibiting a similar relative order.

On Dataset 3, the resulting DSC values, shown in Table 1, are lower than those for Dataset 2. This difference is mainly caused by the fact that Dataset 3 provides pixel-level annotations, whereas Dataset 2 only includes nuclei center annotations. The computation times for AR and ZZ are shorter due to the smaller image size ( $512 \times 512$  vs.  $600 \times 600$  in Dataset 2). SP achieves a DSC improvement of 3.62 over SAM, despite being roughly twice as slow as SAM in the segmentation process. The results also show that SP achieves again the highest DSC performance (76.62), outperforming SMST (DSC 60.63), AR (DSC 61.35), and ZZ (DSC 65.33).

## 8 Conclusion

Global metrics, such as the variance-based energies in the Chan–Vese model [6] and the SMST framework [38], effectively suppress local noise but remain sensitive to global intensity inhomogeneities. In contrast, local region-based models, including AR [22] and ZZ [23], improve robustness to inhomogeneity at the cost of increased computational complexity and a limited global receptive field. We proposed a hierarchical segmentation approach that combines superpixel representations with OT-based region comparison. The two-stage structure enables a consistent use of distributional distances across scales, while reducing the complexity of region interactions and preserving meaningful boundaries. This formulation seems particularly well suited to images with strong intensity inhomogeneity.

Experiments show that the proposed method achieves higher segmentation accuracy than the considered classical and variational approaches, while being up to an order of magnitude faster than level-set methods. Its runtime remains competitive with fast deep-learning-based approaches such as SAM. Segmenting objects with weak boundaries or intensity distributions close to the background remains a challenge.

**Acknowledgements.** This work was partially supported by the National Key R&D Program of China 2021YFA1003003; the National Natural Science Foundation of China 61936002, T2225012; the program of China Scholarships Council 202307300007; and the Engineering and Physical Sciences Research Council (EPSRC grant EP/X035883/1).

## Declarations

- **Conflict of interest** The authors declare no conflict of interest.
- **Data availability** The datasets analyzed in this study are publicly available and cited in the manuscript. All images generated in the course of this work will be provided as supplementary material.
- **Author Contributions** J.H. developed the theory, implemented the code, performed the computations and simulations, and wrote the first draft of the manuscript. A.A., K.C., and N.L. guided, supervised, and reviewed the findings of this work. All authors conceived the presented idea, discussed the results, and contributed to the final manuscript.

## References

- [1] Wang, Z., Ma, B., Zhu, Y.: Review of level set in image segmentation. *Archives of Computational Methods in Engineering* **28**(4), 2429–2446 (2021)
- [2] Yu, H., He, F., Pan, Y.: A survey of level set method for image segmentation with intensity inhomogeneity. *Multimedia Tools and Applications* **79**(39), 28525–28549 (2020)
- [3] Biswas, S., Hazra, R.: State-of-the-art level set models and their performances in image segmentation: a decade review. *Archives of Computational Methods in Engineering* **29**(4), 2019–2042 (2022)
- [4] Kang, S.H., Tai, X.-C., Zhu, W.: Survey of fast algorithms for Euler’s elastica-based image segmentation. In: Kimmel, R., Tai, X.-C. (eds.) *Processing, Analyzing and Learning of Images, Shapes, and Forms: Part 2. Handbook of Numerical Analysis*, vol. 20, pp. 533–552. Elsevier, Amsterdam (2019)
- [5] Mumford, D.B., Shah, J.: Optimal approximations by piecewise smooth functions and associated variational problems. *Communications on Pure and Applied Mathematics* **45**(5), 577–685 (1989)

- [6] Chan, T.F., Vese, L.A.: Active contours without edges. *IEEE Transactions on Image Processing* **10**(2), 266–277 (2001)
- [7] Wang, X.-F., Huang, D.-S., Xu, H.: An efficient local Chan–Vese model for image segmentation. *Pattern Recognition* **43**(3), 603–618 (2010)
- [8] Li, C., Kao, C.-Y., Gore, J.C., Ding, Z.: Implicit active contours driven by local binary fitting energy. In: 2007 IEEE Conference on Computer Vision and Pattern Recognition, pp. 1–7 (2007). IEEE
- [9] Li, N., Liu, F., Li, J., Yang, J., Zheng, T.: A variational method using Riemannian metric for SAR image segmentation. In: 2017 IEEE International Geoscience and Remote Sensing Symposium (IGARSS), pp. 787–790 (2017). IEEE
- [10] Lenglet, C., Rousson, M., Deriche, R., Faugeras, O., Lehericy, S., Ugurbil, K.: A Riemannian approach to diffusion tensor images segmentation. In: Biennial International Conference on Information Processing in Medical Imaging, pp. 591–602 (2005). Springer
- [11] Li, C., Huang, R., Ding, Z., Gatenby, J.C., Metaxas, D.N., Gore, J.C.: A level set method for image segmentation in the presence of intensity inhomogeneities with application to MRI. *IEEE Transactions on Image Processing* **20**(7), 2007–2016 (2011)
- [12] Min, L., Cui, Q., Jin, Z., Zeng, T.: Inhomogeneous image segmentation based on local constant and global smoothness priors. *Digital Signal Processing* **111**, 102989 (2021)
- [13] Caselles, V., Kimmel, R., Sapiro, G.: Geodesic active contours. *International Journal of Computer Vision* **22**(1), 61–79 (1997)
- [14] Liu, C., Liu, W., Xing, W.: A weighted edge-based level set method based on multi-local statistical information for noisy image segmentation. *Journal of Visual Communication and Image Representation* **59**, 89–107 (2019)
- [15] Yu, H., He, F., Pan, Y.: A novel segmentation model for medical images with intensity inhomogeneity based on adaptive perturbation. *Multimedia Tools and Applications* **78**(9), 11779–11798 (2019)
- [16] Zhu, W., Tai, X.-C., Chan, T.: Image segmentation using Euler’s elastica as the regularization. *Journal of Scientific Computing* **57**, 414–438 (2013)
- [17] Lei, N., Huang, J., Chen, K., Ren, Y., Saucan, E., Wang, Z., Shang, Y.: Ricci curvature based volumetric segmentation. *Image and Vision Computing*, 105192 (2024)
- [18] Huang, J., Chen, K., Alpers, A., Lei, N.: Ricci curvature tensor-based volumetric

segmentation. *International Journal of Computer Vision*, 1–22 (2025)

- [19] Vese, L.A., Chan, T.F.: A multiphase level set framework for image segmentation using the Mumford and Shah model. *International Journal of Computer Vision* **50**, 271–293 (2002)
- [20] Wang, L., He, L., Mishra, A., Li, C.: Active contours driven by local Gaussian distribution fitting energy. *Signal Processing* **89**(12), 2435–2447 (2009)
- [21] Zhang, K., Song, H., Zhang, L.: Active contours driven by local image fitting energy. *Pattern Recognition* **43**(4), 1199–1206 (2010)
- [22] Ali, H., Rada, L., Badshah, N.: Image segmentation for intensity inhomogeneity in presence of high noise. *IEEE Transactions on Image Processing* **27**(8), 3729–3738 (2018)
- [23] Zhang, K., Zhang, L., Lam, K.-M., Zhang, D.: A level set approach to image segmentation with intensity inhomogeneity. *IEEE Transactions on Cybernetics* **46**(2), 546–557 (2015)
- [24] Liu, C., Liu, W., Xing, W.: An improved edge-based level set method combining local regional fitting information for noisy image segmentation. *Signal Processing* **130**, 12–21 (2017)
- [25] Roberts, M., Chen, K., Irion, K.L.: A convex geodesic selective model for image segmentation. *Journal of Mathematical Imaging and Vision* **61**(4), 482–503 (2019)
- [26] Sussman, M., Smereka, P., Osher, S.: A level set approach for computing solutions to incompressible two-phase flow. *Journal of Computational Physics* **114**(1), 146–159 (1994)
- [27] Li, C., Xu, C., Gui, C., Fox, M.D.: Distance regularized level set evolution and its application to image segmentation. *IEEE Transactions on Image Processing* **19**(12), 3243–3254 (2010)
- [28] Fiedler, M., Alpers, A.: Power-SLIC: Fast superpixel segmentations by diagrams. arXiv preprint arXiv:2012.11772 (2020)
- [29] Panaretos, V.M., Zemel, Y.: Statistical aspects of Wasserstein distances. *Annual Review of Statistics and its Application* **6**(1), 405–431 (2019)
- [30] Hao, M., Shi, W., Deng, K., Feng, Q.: Superpixel-based active contour model for unsupervised change detection from satellite images. *International Journal of Remote Sensing* **37**(18), 4276–4295 (2016)
- [31] Zhou, X., Chen, K., Zhou, Q.: Superpixel-based level set tracking by integrating appearance and motion. In: 2017 IEEE Visual Communications and Image

Processing (VCIP), pp. 1–4 (2017). IEEE

- [32] Zhou, X., Li, X., Chin, T.-J., Suter, D.: Superpixel-driven level set tracking. In: 2012 19th IEEE International Conference on Image Processing, pp. 409–412 (2012). <https://doi.org/10.1109/ICIP.2012.6466882>
- [33] Zhou, X., Li, X., Hu, W.: Learning a superpixel-driven speed function for level set tracking. *IEEE Transactions on Cybernetics* **46**(7), 1498–1510 (2015)
- [34] Li, Y., Pan, H., Wu, X., Liu, Y., Pang, S., Zhu, L.: Fast two-cycle level set tracking with interactive superpixel segmentation and its application in image retrieval. *IEEE Access* **7**, 159930–159942 (2019)
- [35] Xia, M., Yan, W., Huang, Y., Guo, Y., Zhou, G., Wang, Y.: Ivus image segmentation using superpixel-wise fuzzy clustering and level set evolution. *Applied Sciences* **9**(22), 4967 (2019)
- [36] Liu, G., Jiang, Y., Chang, B., Liu, D.: Superpixel-based active contour model via a local similarity factor and saliency. *Measurement* **188**, 110442 (2022)
- [37] Liu, Z., Zhang, L.: A superpixel-level active contour model with global and local constrains. In: International Conference on Automatic Control and Artificial Intelligence (ACAI 2012), pp. 301–304 (2012). IET
- [38] Wang, M., Dong, Z., Cheng, Y., Li, D.: Optimal segmentation of high-resolution remote sensing image by combining superpixels with the minimum spanning tree. *IEEE Transactions on Geoscience and Remote Sensing* **56**(1), 228–238 (2017)
- [39] Yin, W., Yang, J.: Sub-pixel vs. super-pixel-based greenspace mapping along the urban–rural gradient using high spatial resolution Gaofen-2 satellite imagery: a case study of Haidian District, Beijing, China. *International Journal of Remote Sensing* **38**(22), 6386–6406 (2017) <https://doi.org/10.1080/01431161.2017.1354266>
- [40] Xiang, D., Zhang, F., Zhang, W., Tang, T., Guan, D., Zhang, L., Su, Y.: Fast pixel-superpixel region merging for sar image segmentation. *IEEE Transactions on Geoscience and Remote Sensing* **59**(11), 9319–9335 (2020)
- [41] Li, P., Wang, Q.: Variational earth mover’s distance for image segmentation. In: 2013 Seventh International Conference on Image and Graphics, pp. 236–242 (2013). IEEE
- [42] Huang, J., Chen, K., Alpers, A., Lei, N.: Graph-based inhomogeneity image segmentation with the optimal transport metric. In: Proceedings of the IEEE International Conference on Bioinformatics and Biomedicine (BIBM) (2025). IEEE. In press

- [43] De Loera, J.A., Kim, E.D.: Combinatorics and geometry of transportation polytopes: An update. *Discrete Geometry and Algebraic Combinatorics* **625**, 37–76 (2013)
- [44] Villani, C.: *Optimal Transport: Old and New* vol. 338. Springer, Heidelberg (2008)
- [45] Peyré, G., Cuturi, M.: Computational optimal transport: With applications to data science. *Foundations and Trends® in Machine Learning* **11**(5-6), 355–607 (2019)
- [46] Friesecke, G.: *Optimal Transport: A Comprehensive Introduction to Modeling, Analysis, Simulation, Applications*. SIAM, Philadelphia (2024)
- [47] Kirillov, A., Mintun, E., Ravi, N., Mao, H., Rolland, C., Gustafson, L., Xiao, T., Whitehead, S., Berg, A.C., Lo, W.-Y., Piotr, D., Girshick, R.: Segment anything. In: *Proceedings of the IEEE/CVF International Conference on Computer Vision*, pp. 4015–4026 (2023)
- [48] Dosovitskiy, A., Beyer, L., Kolesnikov, A., Weissenborn, D., Zhai, X., Unterthiner, T., Dehghani, M., Minderer, M., Heigold, G., Gelly, S., *et al.*: An image is worth 16x16 words: Transformers for image recognition at scale. In: *International Conference on Learning Representations* (2020)
- [49] Ali, M., Wu, T., Hu, H., Luo, Q., Xu, D., Zheng, W., Jin, N., Yang, C., Yao, J.: A review of the segment anything model (SAM) for medical image analysis: Accomplishments and perspectives. *Computerized Medical Imaging and Graphics* **119**, 102473 (2025) <https://doi.org/10.1016/j.compmedimag.2024.102473>
- [50] Ji, W., Li, J., Bi, Q., Liu, T., Li, W., Cheng, L.: Segment anything is not always perfect: An investigation of SAM on different real-world applications. *Machine Intelligence Research* **21**, 617–630 (2024) <https://doi.org/10.1007/s11633-023-1385-0>
- [51] Jiani, L.E., Filali, S.E., Benlahmer, E.H.: Exploring segment anything model applications for medical imaging. In: *2024 4th International Conference on Innovative Research in Applied Science, Engineering and Technology (IRASET)*, pp. 1–6 (2024). <https://doi.org/10.1109/IRASET60544.2024.10548751>
- [52] Stutz, D., Hermans, A., Leibe, B.: Superpixels: An evaluation of the state-of-the-art. *Computer Vision and Image Understanding* **166**, 1–27 (2018)
- [53] Wang, M., Liu, X., Gao, Y., Ma, X., Soomro, N.Q.: Superpixel segmentation: A benchmark. *Signal Processing: Image Communication* **56**, 28–39 (2017)
- [54] Achanta, R., Shaji, A., Smith, K., Lucchi, A., Fua, P., Süstrunk, S.: SLIC superpixels compared to state-of-the-art superpixel methods. *IEEE Transactions on*

- [55] Lloyd, S.: Least squares quantization in PCM. *IEEE Transactions on Information Theory* **28**(2), 129–137 (1982)
- [56] MacQueen, J.: Some methods for classification and analysis of multivariate observations. In: *Proceedings of the Fifth Berkeley Symposium on Mathematical Statistics and Probability*, vol. 1, pp. 281–297 (1967). Oakland, CA, USA
- [57] Robertson, A.R.: The CIE 1976 color-difference formulae. *Color Research & Application* **2**(1), 7–11 (1977)
- [58] Altendorf, H., Latourte, F., Jeulin, D., Faessel, M., Saintoyant, L.: 3D reconstruction of a multiscale microstructure by anisotropic tessellation models. *Image Analysis and Stereology* **33**(2), 121–130 (2014)
- [59] Alpers, A., Brieden, A., Gritzmann, P., Lyckegaard, A., Poulsen, H.F.: Generalized balanced power diagrams for 3D representations of polycrystals. *Philosophical Magazine* **95**(9), 1016–1028 (2015)
- [60] Aurenhammer, F., Klein, R., Lee, D.-T.: *Voronoi Diagrams and Delaunay Triangulations*. World Scientific Publishing Company, Singapore (2013)
- [61] Alpers, A., Fiedler, M., Gritzmann, P., Klemm, F.: Dynamic grain models via fast heuristics for diagram representations. *Philosophical Magazine* **103**(10), 948–968 (2023)
- [62] Guo, D.: Regionalization with dynamically constrained agglomerative clustering and partitioning (redcap). *International Journal of Geographical Information Science* **22**(7), 801–823 (2008)
- [63] Drăguț, L., Tiede, D., Levick, S.R.: ESP: a tool to estimate scale parameter for multiresolution image segmentation of remotely sensed data. *International Journal of Geographical Information Science* **24**(6), 859–871 (2010)
- [64] Cormen, T.H., Leiserson, C.E., Rivest, R.L., Stein, C.: *Introduction to Algorithms*, 3rd edn. MIT Press, Massachusetts (2009)
- [65] Papadimitriou, C.H.: *Computational Complexity*. Addison-Wesley, Reading, MA (1994)
- [66] Diestel, R.: *Graph Theory*, 5th edn. Springer, Heidelberg (2017)
- [67] Orlin, J.B.: A faster strongly polynomial minimum cost flow algorithm. *Operations Research* **41**(2), 338–350 (1993)
- [68] Bonneel, N., Van De Panne, M., Paris, S., Heidrich, W.: Displacement interpolation using Lagrangian mass transport. In: *Proceedings of the 2011 SIGGRAPH*

Asia Conference, pp. 1–12 (2011)

[69] Bonneel, N.: Network Simplex Optimal Transport Solver. [https://github.com/nbonneel/network\\_simplex](https://github.com/nbonneel/network_simplex). Accessed: 2026-01-19 (2015)

[70] Higham, N.J.: Accuracy and Stability of Numerical Algorithms. SIAM, Philadelphia (2002)

[71] Hoang, V.K.M.: Systemic Mastocytosis Associated with a Hematologic Neoplasm in a Patient with Multiple Abnormal Hem. <https://imagebank.hematology.org/imageset/60231/systemic-mastocytosis-associated-with-a-hematologic-neoplasm-in-a-patient-with-multiple-abnormal-hem>. Accessed: 2026-01-19 (2020)

[72] Chan, J.K.: The wonderful colors of the hematoxylin–eosin stain in diagnostic surgical pathology. International Journal of Surgical Pathology **22**(1), 12–32 (2014)

[73] Wienert, S., Heim, D., Saeger, K., Stenzinger, A., Beil, M., Hufnagl, P., Dietel, M., Denkert, C., Klauschen, F.: Detection and segmentation of cell nuclei in virtual microscopy images: a minimum-model approach. Scientific Reports **2**(1), 503 (2012)

[74] Naylor, P., Laé, M., Reyal, F., Walter, T.: Segmentation of nuclei in histopathology images by deep regression of the distance map. IEEE Transactions on Medical Imaging **38**(2), 448–459 (2018)

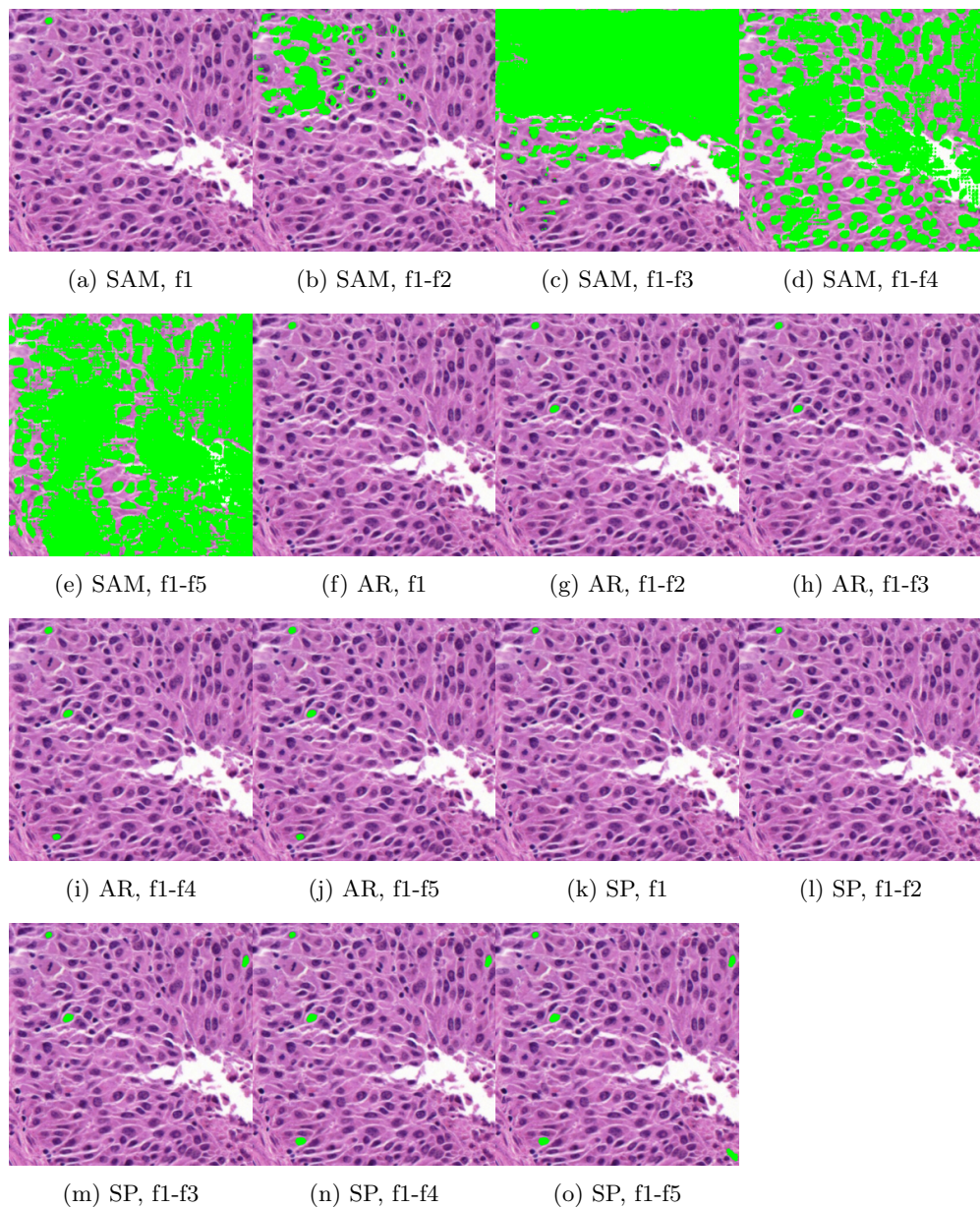


**Fig. 6:** Selective segmentation results for the image in Fig. 5a using background marker b1 and incrementally added foreground markers: f1, f1-f2, f1-f3, f1-f4, and f1-f5. (a–e) SAM, (f–j) AR, (k–o) SP.

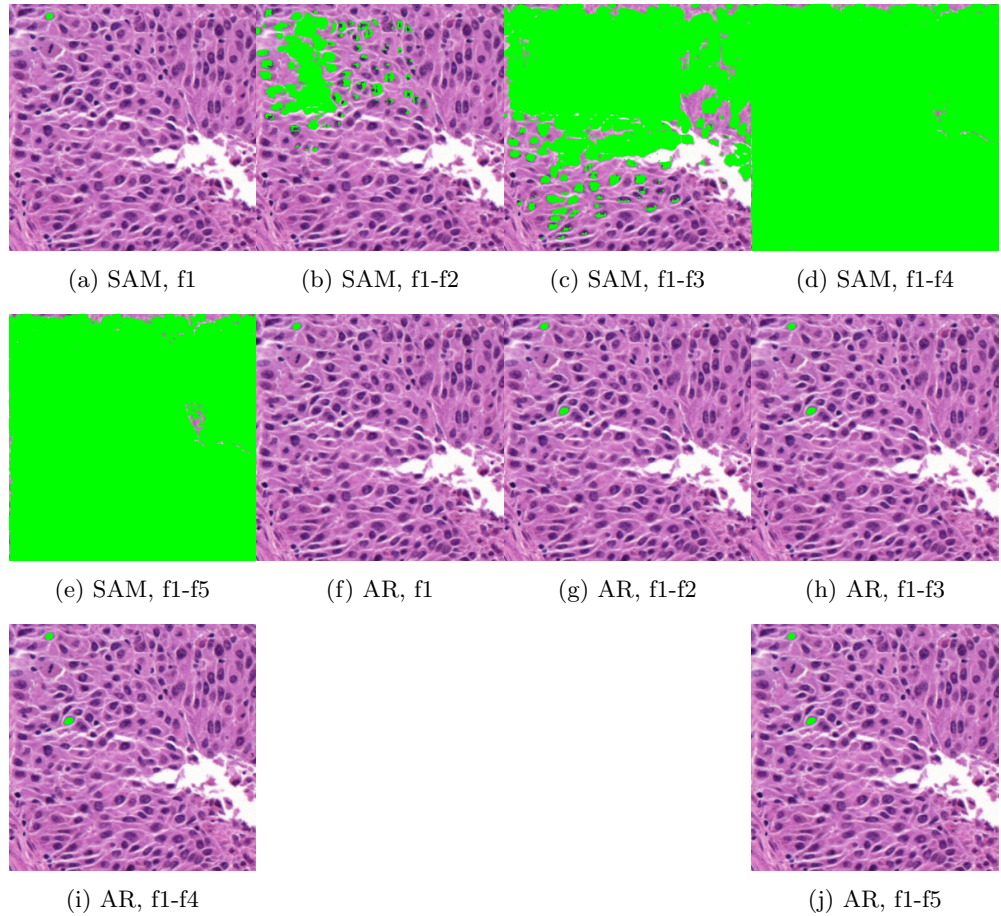


**Fig. 7:** Selective segmentation results for the image in Fig. 5c using background marker b1 and incrementally added foreground markers: f1, f1-f2, f1-f3, f1-f4, and f1-f5. (a–e) SAM, (f–j) AR.

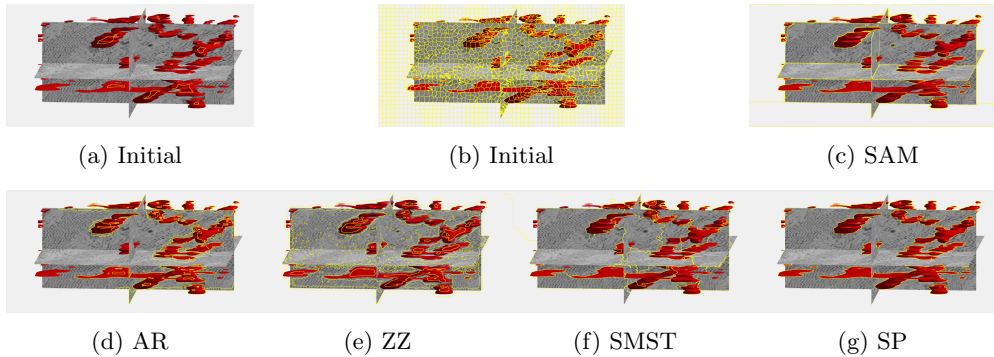


**Fig. 8:** Comparison of unsupervised segmentation models on Dataset 1. (a) and (b) show the intial level sets and superpixel, respectively: AR and ZZ in (a) (yellow curves, computation times  $\infty$ ), SMST and SP in (b) (yellow curves, 0.42s). (c–g) show segmentation results (yellow curves) from SAM, AR, ZZ, SMST, and SP, respectively.

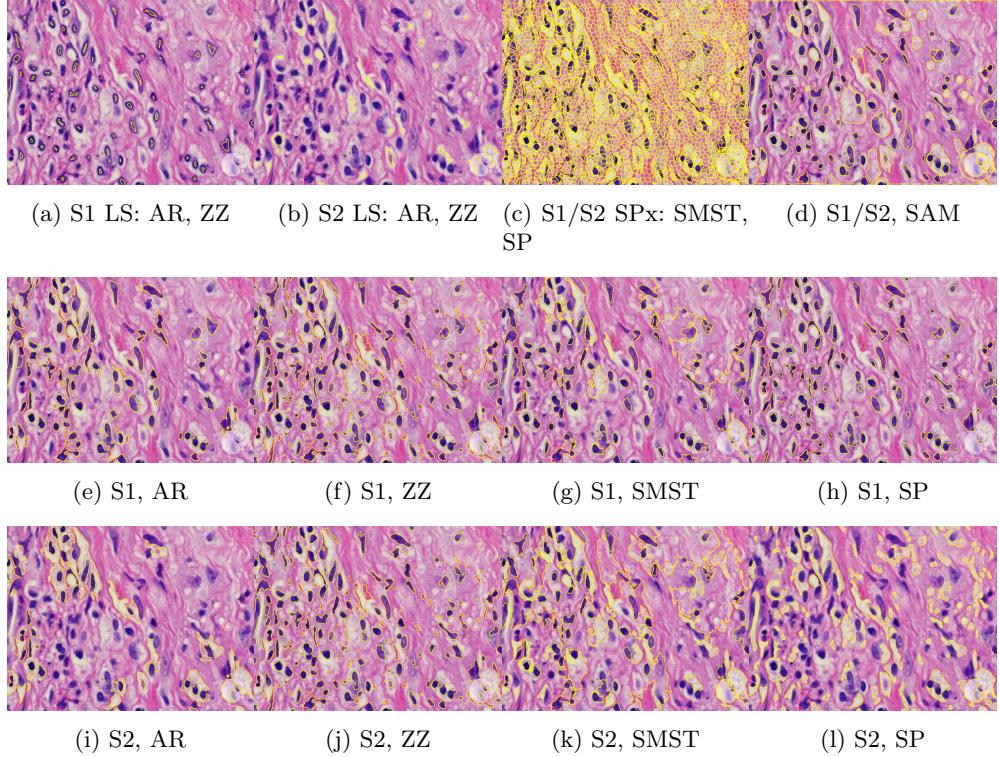


**Fig. 9:** Unsupervised segmentation of the image in Fig. 1b for two structures: purple cells (S1) and white cytoplasm (S2). Initializations via level sets (LS) for AR and ZZ are shown in (a, b); 4000 superpixels for SMST and SP in (c) (red channel for S1, remaining channels for S2). SAM does not allow separate-channel segmentation; its overall output is in (d). Results for S1 are in (e–h) and for S2 in (i–l). Computation times (S1/S2, in seconds): AR 829.51/570.32, ZZ 4304.50/4470.56, SMST 0.38/0.38, SP 5.98/4.26; superpixels in (c) computed in 0.17s, SAM in (d) in 7.42s.

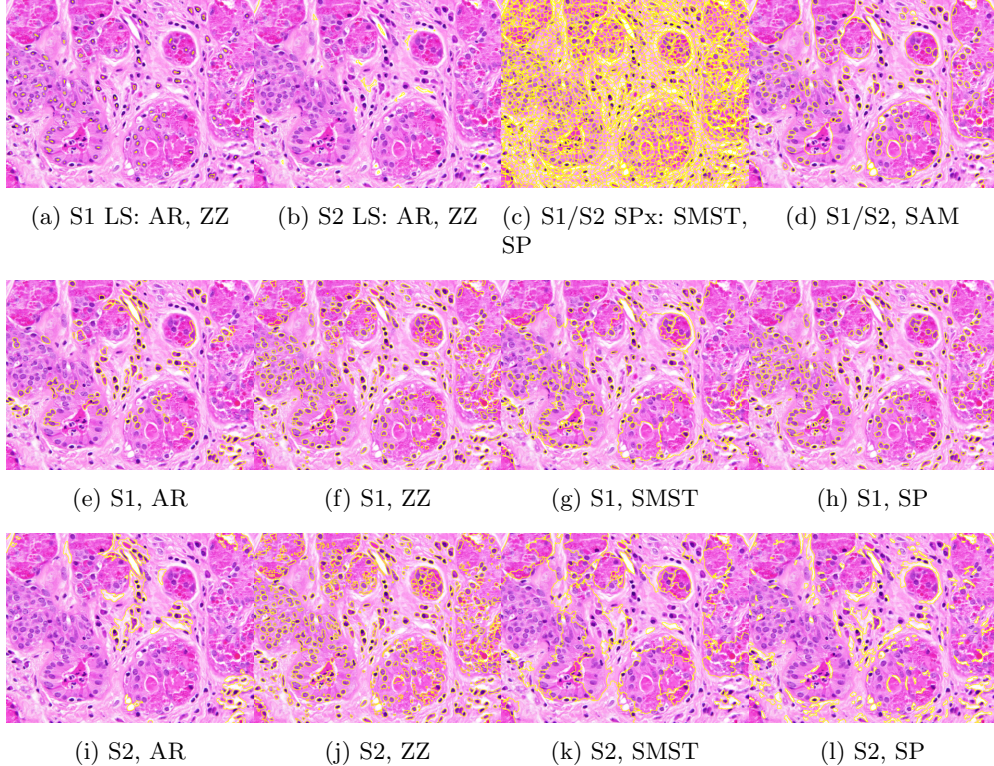
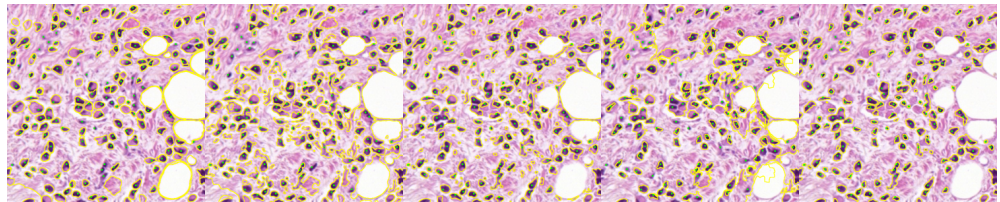
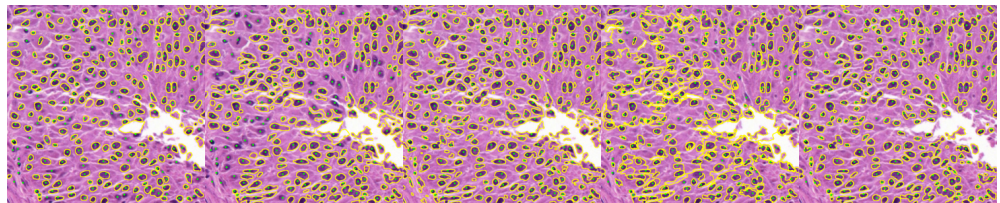


**Fig. 10:** Unsupervised segmentation of the image in Fig. 1c for two structures: purple cells (S1) and white cytoplasm (S2). Initializations via level sets (LS) for AR and ZZ are shown in (a, b); 6000 superpixels for SMST and SP in (c) (red channel for S1, remaining channels for S2). SAM does not allow separate-channel segmentation; its overall output is in (d). Results for S1 are in (e–h) and for S2 in (i–l). Computation times (S1/S2, in seconds): AR 461.85/474.46, ZZ 2423.73/2434.59, SMST 0.42/0.38, SP 42.31/12.51; superpixels in (c) computed in 0.14s, SAM in (d) in 7.47s.



(a) S3, SAM (7.62/81.88) (b) S3, AR (234.69/64.32) (c) S3, ZZ (1195.00/70.69) (d) S3, SMST (0.43/82.39) (e) S3, SP (4.32/86.77)



(f) S4, SAM (7.48/83.64) (g) S4, AR (428.36/76.72) (h) S4, ZZ (2232.16/84.36) (i) S4, SMST (0.46/79.31) (j) S4, SP (15.75/89.33)

**Fig. 11:** Segmentation of two images from the quantitative comparison on Dataset 2 (S3 and S4, Figs. 1d and 1e); brackets show segmentation time (s) / DSC.